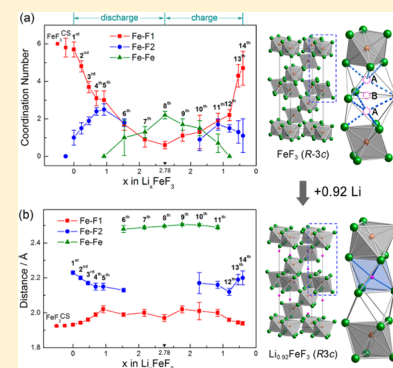


In Situ Electrochemical XAFS Studies on an Iron Fluoride High-Capacity Cathode Material for Rechargeable Lithium Batteries

Wei Zhang,[†] Paul N. Duchesne,[§] Zheng-Liang Gong,^{||} Shun-Qing Wu,[⊥] Lin Ma,[†] Zheng Jiang,[#] Shuo Zhang,[#] Peng Zhang,^{*,§} Jin-Xiao Mi,[‡] and Yong Yang^{*,†,||}[†]State Key Lab of Physical Chemistry of Solid Surfaces and Department of Chemistry and [‡]Department of Materials Science and Engineering, Xiamen University, Xiamen 361005, China[§]Department of Chemistry, Dalhousie University, Halifax B3H 4R2, Canada^{||}School of Energy Research and [⊥]Department of Physics and Institute of Theoretical Physics and Astrophysics, Xiamen University, Xiamen 361005, China[#]Shanghai Synchrotron Radiation Facility, Shanghai Institute of Applied Physics, Chinese Academy of Science, Shanghai 201204, China

Supporting Information

ABSTRACT: The reactions and structural evolution of FeF₃ during cell cycling are investigated in an in situ cell by using Fe K-edge X-ray absorption fine-structure (XAFS) spectroscopy. The results of X-ray absorption near-edge structure spectroscopic analysis demonstrate that there are three stages in the reaction of FeF₃ with Li: (1) a two-phase intercalation reaction in the range of $x = 0$ to 0.46 Li, (2) a single-phase intercalation reaction in the range of $x = 0.46$ to 0.92 Li, and (3) a conversion reaction in the range of $x = 0.92$ to 2.78 Li. The coordination numbers (CNs) and bond lengths of the Fe–F bonds or Fe–Fe bonds for the lithiated FeF₃ are obtained by performing XAFS fitting. The splitting trends of the Fe–F bond lengths and the Fe–F CNs in the range of $x = 0$ to 0.92 Li support the proposal that R-3c-structured FeF₃ is transformed into R3c-structured Li_{0.92}FeF₃ after the intercalation of 0.92 equiv. of Li, and that the intermediate Li_{0.46}FeF₃ may be R3-structured. The small Fe–Fe CN of Li_{2.78}FeF₃ indicates that the average diameter of the Fe crystallites formed during discharge is <1 nm.



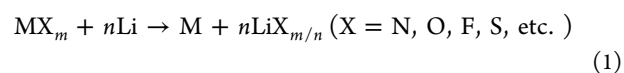
1. INTRODUCTION

Cathode materials based on intercalation reactions (LiCoO₂, LiFePO₄, LiMn₂O₄, etc.) exhibit good electrochemical performance in terms of cycling stability and rate capability; however, they possess limited specific capacities, determined mainly by the limited number of intercalated lithium ions that may be removed from them without inducing structural collapse. In contrast, cathode materials based on conversion reactions show very large specific capacities due to nearly all of the oxidation states of the active materials being utilized.^{1–4} Among the M_xN_y (M = Co, Fe, Ni, Cu, etc.; N = F, O, S, N, etc.) conversion materials, metal fluorides offer the highest operating voltages and have significant potential to be developed as cathode materials for rechargeable Li batteries.⁵

Fluoride-based electrode materials for advanced energy-storage devices and the utilization of metal fluorides as cathode materials can be traced to the late 1960s.⁴ However, the first application of iron(III) fluoride (FeF₃) in rechargeable lithium batteries was reported in 1997 by Arai.⁶ Although the reported discharge was not high (~140 mA h g^{−1} for the first cycle and 80 mA h g^{−1} for the second cycle, between 2.0 and 4.5 V, with a constant-current density of 0.2 mA cm^{−2}), it still attracted tremendous interest within the field of battery electrode

materials; such iron-based materials provide some distinct advantages, including low cost, low toxicity, and the utilization of three lithium ions resulting in a large theoretical capacity of 712 mA h g^{−1}. FeF₃ is considered to be one of the most promising fluoride materials used to maximize the energy density of rechargeable electrochemical cells; unfortunately, the poor electronic conductivity of FeF₃, associated with the large band gap (5.96 eV),⁷ leads to poorer electrochemical performance. Consequently, many efforts to improve the electrochemical performance of FeF₃-based materials are focused on increasing the electronic conductivity and reducing the particle size and have demonstrated effectiveness in improving electrochemical reversibility and rate capability.^{2–4,8–15}

Tarascon et al.¹ and Li et al.¹⁶ proposed that the reaction of conversion materials with lithium proceeds as follows:

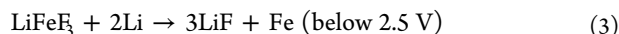
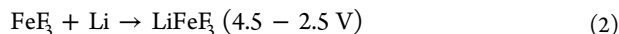


Received: February 1, 2013

Revised: May 10, 2013

Published: May 13, 2013

Badway and coworkers^{3,9} went a step further and proposed that reaction 1 proceeds in two steps: an intercalation reaction in the range of 4.5–2.5 V and a subsequent conversion reaction in the range below 2.5 V, as follows:



In addition, closer inspection of data from X-ray diffraction (XRD) and cell discharge under galvanostatic intermittent titration technique (GITT) measurements revealed that there is a transformation from two-phase intercalation to single-phase topotactic intercalation during the first step of this reaction. Later, Yamakawa et al.⁵ found further proof of this transformation using magic-angle-spinning nuclear magnetic resonance (MAS NMR) spectroscopy, as Li NMR data indicated a progressive increase in the concentration of Fe^{2+} when the amount of intercalated Li was >0.5 equiv.

Investigation of the structural evolution of FeF_3 during cycling presents a greater challenge. Badway et al.^{3,9} determined using in situ and ex situ XRD that the intensity of Bragg peaks varied significantly during the first lithiation reaction, especially in the range of $x = 0$ to 1.0 Li; the sharp decrease in the (012) peak intensity is thought to be related to the alteration of the Fe array in FeF_3 . Selected area electron diffraction (SAED) characterization revealed the reformation of a metal fluoride with FeF_2 -like structure when recharged to 4.5 V. Yamakawa et al.⁵ proposed, on the basis of the pair distribution function (PDF) analysis, that the $\text{Li}_{0.5}\text{FeF}_3$ phase is of a rutile-like structure at least locally.

X-ray absorption fine-structure (XAFS) is a powerful technique for characterizing the structures and electronic states of materials and has been successfully applied to many research fields, including biology, chemistry, electronics, geophysics, metallurgy, and materials science.^{17–20} The application of XAFS in the field of electrode materials for lithium batteries has also been studied by many groups in recent decades.^{10,21–29} To the best of our knowledge, besides BiF_3 ²⁸ and CuF_2 ,^{10,29} few metal fluorides used as cathode materials have been investigated using XAFS techniques. Herein, we report the results regarding the structural evolution of FeF_3 during cycling by using Fe K-edge XAFS spectroscopy.

2. EXPERIMENTAL SECTION

The synthesis and physical characterization of anhydrous FeF_3 using XRD and SEM, and the preparation of the electrode material have been described in detail in a previous publication;¹⁴ additional details have also been included in the Supporting Information. The FeF_3/C composite was prepared by high-energy mechanomilling anhydrous FeF_3 with 15 wt % carbon black (Super P) for 4 h at 500 rpm. A total of 1 g of material was loaded into an agate milling cell with zirconia balls. The milling cell was sealed and reopened after milling in an argon-filled glovebox, thus protecting the composite from moisture. The cathodes for ex situ XRD measurement were obtained by disassembling the CR2025 coin-type electrochemical cells in an Ar-filled glovebox, rinsing the cathode with dimethyl carbonate (DMC), and drying it under vacuum.

The XRD data were collected using Panalytical X'pert Pro diffractometer (PANalytical, Netherlands), with a Cu $K\alpha$ radiation source (wavelength, $\lambda = 1.54056 \text{ \AA}$) operated at 40 kV and 30 mA, a step size of 0.00835° , and a counting time of

30 s per step. Rietveld refinements were performed using the General Structure Analysis System (GSAS) program³⁰ to obtain crystallographic parameters for each sample. Two types of electrochemical cells were used in this study: a CR2025 coin-type cell for ex situ XRD measurements and a special in situ cell for XAFS measurements (similar to Rosciano's 'coffee bag' cell;³¹ see the Supporting Information for details). The electrochemical cell was assembled in an argon-filled glovebox with the prepared cathode, a lithium anode, a Celgard 2300 separator, and 1 M LiPF_6 in ethylene carbonate (EC) and DMC (1:1 EC/DMC, v/v) electrolyte. Cell discharge/charge was carried out at a current rate of 100 mA g^{-1} at room temperature ($\sim 25^\circ\text{C}$) using a Land CT2001A system. Once the in situ cell had been discharged (or charged) to a chosen potential (see Figure 2), charging was halted and XAFS measurements were begun immediately.

The XAFS data at the Fe K-edge were collected at room temperature in transmission mode using ion chamber detectors at beamline BL14W1 of the Shanghai Synchrotron Radiation Facility (SSRF).³² During the measurement, the synchrotron was operated at an energy of 3.5 GeV and a ring current of 150–210 mA. The beamline employed a 38 pole wiggler insertion device as a photon source (flux = 1.9×10^{13} photons s^{-1}) and a Si(111) double-crystal monochromator for wavelength selection (energy resolution, $\Delta E/E = 1.5 \times 10^{-4}$). The focal spot size at the position of the sample was $\sim 0.25 \text{ mm}^2$. The monochromator was detuned to reject higher harmonics of the selected wavelength (harmonic content $<10^{-4}$) and was scanned in energy from 200 eV below to 1000 eV above the Fe K-edge (7111.2 eV)³³ for each measurement. The incident photon energy was calibrated using a standard Fe metal foil just prior to data collection from all lithiated FeF_3 samples; for the in situ XAFS measurement, the electrochemical cell was not allowed to move, so the energy calibration cannot be performed after each scan. Processing and fitting of the XAFS data were performed using WinXAS software.³⁴ We performed the energy calibration using Fe foil only at beginning of the XAFS measurements.

3. RESULTS AND DISCUSSION

The XRD pattern and full pattern refinement of pure FeF_3 are shown in Figure 1a. All Bragg peaks are fully indexed to a rhombohedral structure with the $R\bar{3}c$ space group. Refined structural parameters showed a good fit to the published FeF_3 ICDD standard (00-033-0647), and were identified as follows: $a = b = 5.2239(6) \text{ \AA}$, $c = 13.2854(12) \text{ \AA}$, cell volume = $313.97(10) \text{ \AA}^3$, $wR_p = 3.16\%$, $R_p = 2.59\%$, and $\chi^2 = 1.302$. Scanning electron microscopy (SEM) images show the morphology of pure FeF_3 (see Figure 1b); FeF_3 particles were found to be interconnected, forming a fine network structure with single particle sizes of approximately 100–150 nm.

Figure 2 shows the discharge/charge profile of the FeF_3 cathode for XAFS measurements conducted in the in situ cell. The discharge and charge capacities were found to be 661 and 565 mA h g^{-1} , respectively (calculated based on the mass of FeF_3). Figure 3 shows the X-ray absorption near-edge structure (XANES) spectra of several reference compounds, wherein CS denotes the spectrum of the as-prepared FeF_3/C cathode sheet prior to being assembled into a cell and OCV denotes the spectrum first (see Figure 2) collected at open circuit voltage for the in situ cell. The weaker inflection points in the spectra of FeF_2 and FeF_3 were located at 7111.4 and 7113.2 eV (see the

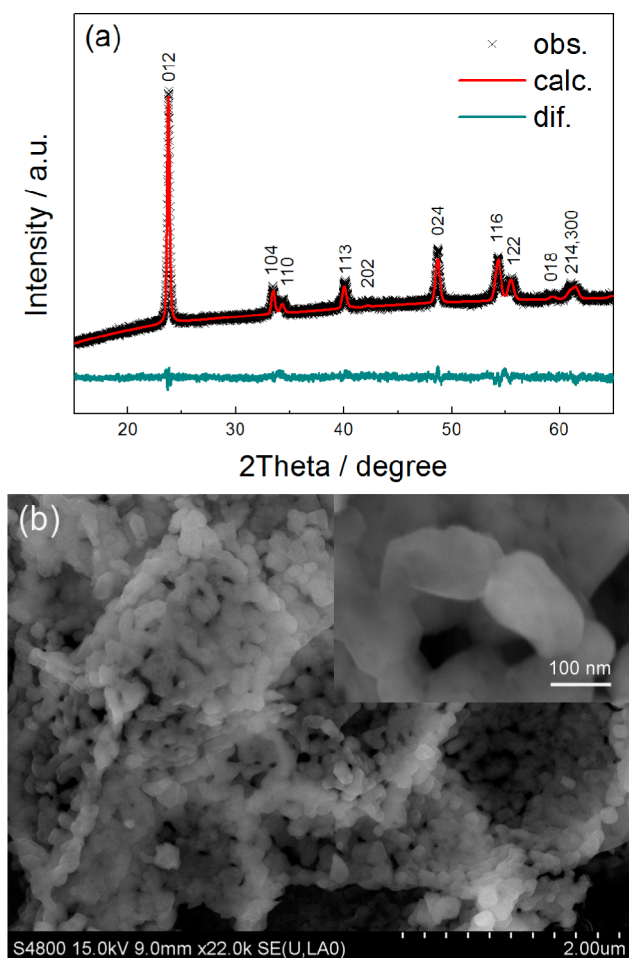


Figure 1. Results of the physical characterization of FeF_3 : (a) observed, calculated, and difference plots for the XRD pattern and (b) representative SEM images.

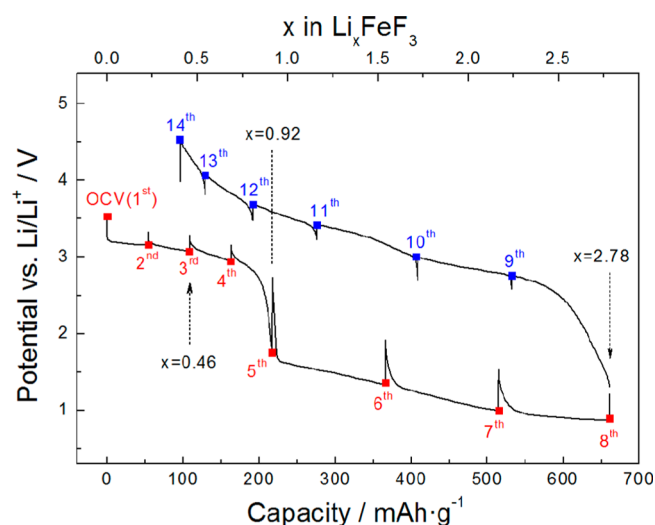


Figure 2. Voltage profiles for the in situ discharge/charge of the FeF_3 cathode. A total of eight XAFS spectra were collected during discharge, and an additional six spectra were collected during the charging process (labeled as 1st–8th and 9th–14th, respectively).

inset in Figure 3), corresponding to the $1s \rightarrow 3d$ electronic transition; the most obvious inflection points in the spectra of FeF_2 and FeF_3 were located at 7122.6 eV and 7129.1 eV,

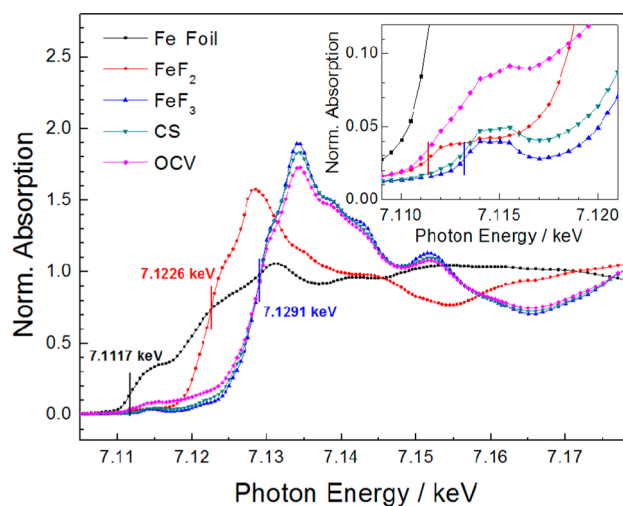


Figure 3. XANES spectra of Fe foil, FeF_2 , FeF_3 , CS, and OCV. The inset shows a close-up of the pre-edge features.

respectively, similar to those obtained by Westre et al. and corresponding to the $1s \rightarrow 4p$ electronic transition.³⁵ These more obvious inflection points were helpful in determining the oxidation state of the FeF_3 cathode at various points of discharge/charge. There was some observed difference in absorption between the CS and OCV spectra; this may be due to intercalation of very small amount of Li into the FeF_3 lattice, as the in situ cell was measured 40 h after being prepared.

The in situ XANES spectra of the FeF_3 cathode during discharge are shown in Figure 4a. Careful inspection indicated distinctive behaviors between spectra 1st–5th and spectra 6th–8th. The spectra 1st–5th shared a unique isosbestic point, while spectra 6th–8th shared a different set of isosbestic points. It is known that the presence of isosbestic points is a quick indication of a direct transformation of reactants to products;^{20,30} therefore, all 14 spectra could be divided into two groups (1st–5th and 6th–8th) based on the two distinct sets of isosbestic points, as shown in Figure 4b,c. According to the XRD results discussed in the following sections, the components of 1st–5th states and 6th–8th states are (FeF_3 and Li_xFeF_3) and (Li_xFeF_3 and Fe), respectively. Moreover, it is important to note that the spectra 1st–5th and spectra 6th–8th shared their characteristic inflection points with FeF_2 and Fe metal, respectively, indicating that Fe^{2+} was formed in a very early stage of discharge and that the Fe metal was formed in the range of $x = 0.92$ to 2.78 Li. These results were precisely consistent with the electrochemical mechanism revealed by reactions 2 and 3. The formation of Fe metal was further supported by ex situ XRD and Fourier transforms of k^3 -weighted XAFS spectra, as discussed later. Close inspection of the XANES data for the lithiated FeF_3 with intercalation of 0 to 0.92 Li atoms revealed that the spectra 1st–3rd shared a unique common intersection point, while the spectra 3rd–5th deviated somewhat from this point. (See the inset in Figure 4b.) A similar phenomenon was also observed by Jain et al. when utilizing XAFS techniques in the investigation of the intercalation of Li into Fe_2O_3 ; they attributed this to a continuous lithium intercalation via a topotactic reaction.³⁶ In short, the fact that spectra 1st–3rd shared an isosbestic point and spectra 3rd–5th did not provided evidence that reaction 2 proceeded via a two-phase process in the range of $x = 0$ to 0.46 Li and via a one-phase process in the range of $x = 0.46$ to 0.92

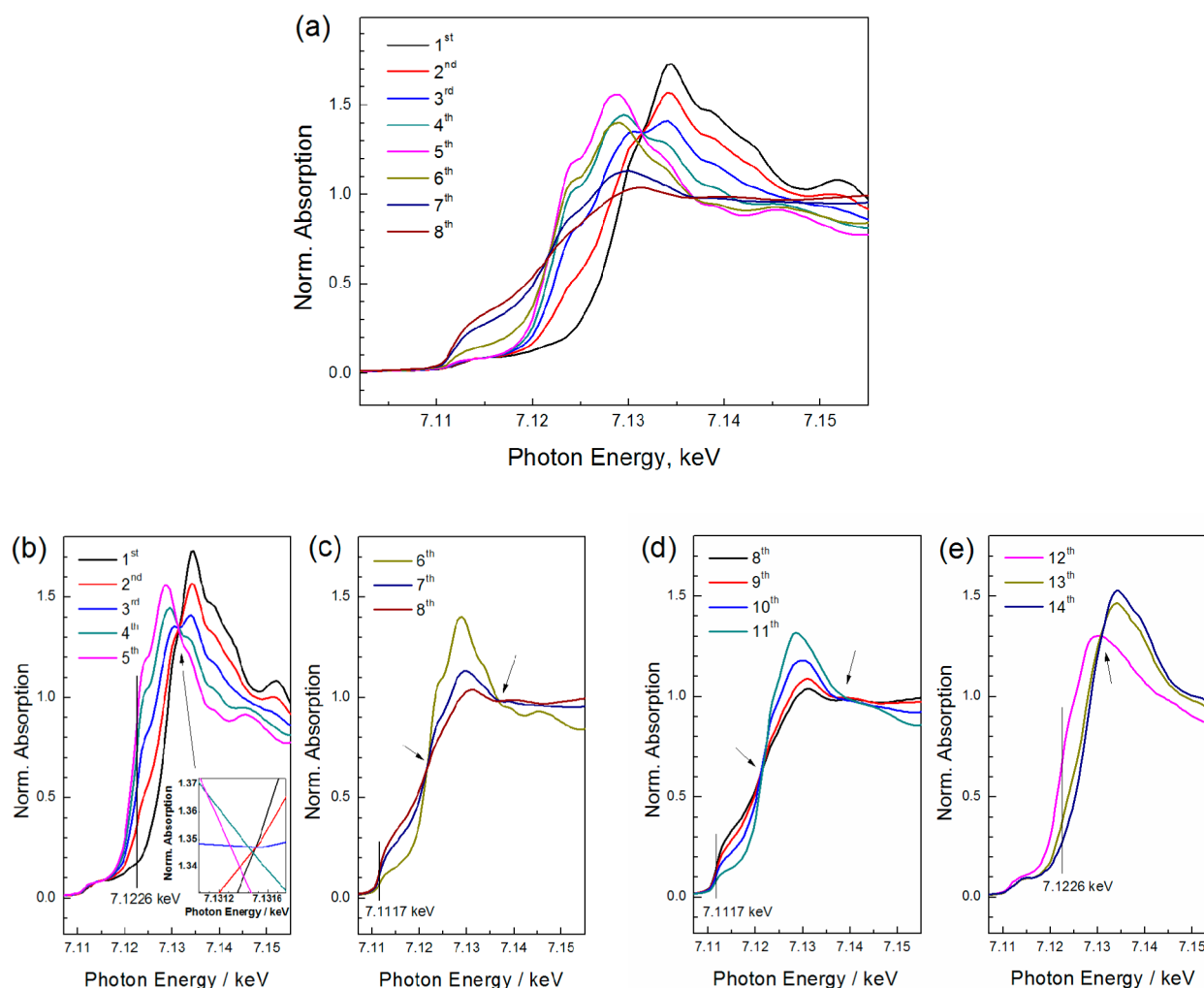


Figure 4. (a) XANES spectra of the lithiated FeF_3 cathode at various points during discharge. These can be divided into two groups: (b) spectra 1st–5th and (c) spectra 6th–8th. The spectra during charge can also be divided into two groups: (d) spectra 8th–11th and (e) spectra 12th–14th. The inset in the bottom of panel b shows an expanded view of the selected area. Arrows are used to indicate isosbestic points; the characteristic inflection points of FeF_3 and Fe foil (i.e., 7.1226 and 7.1117 keV) are also labeled for comparison (b–e).

Li; this is consistent with the results obtained by Badway et al. using cell discharge under GITT protocols and Yamakawa et al. using MAS NMR.^{3,5} The presence or absence of isosbestic points revealed the reaction schemes corresponding to the two different regions ($x = 0$ to 0.92 Li and $x = 0.92$ to 2.78 Li). In fact, the linear combination was also effective in doing this job. (See the Supporting Information for additional details.)

In the following section, the structural evolution of the cathode material will be discussed via analysis of ex situ XRD and XAFS spectra. Figure 5 shows the ex situ XRD patterns of the FeF_3 cathodes at specific states of discharge/charge, which are similar to those states (shown in Figure 2) chosen for in situ XAFS measurements. Two Bragg peaks, located at 38.5° and 44.7° , were indexed to the (110) and (200) peaks of Al, respectively (derived from the Al current collector). The crystallite size of the FeF_3 in the as-prepared cathode was 16.3 nm, as determined via application of the Scherrer formula to the (012) Bragg peak for scan first. During discharge from $x = 0$ to 0.46 Li, the intensities of the Bragg peaks corresponding to (104), (110), and especially (012) lattice planes changed significantly, while that of the (113) peak changed little. During discharge from $x = 0.46$ to 0.92 Li, there was a considerable increase in the intensity of the peaks (012), (104), and (110)

and a remarkable shift in the positions of all peaks to lower 2θ angles, suggesting the structural similarity between $\text{Li}_{0.46}\text{FeF}_3$ and $\text{Li}_{0.92}\text{FeF}_3$ and an expansion of the unit cell. The reason for the significant intensity change in the (012) peak is, in our opinion, the structural evolution from space group $R\bar{3}c$ (FeF_3) to $R3c$ ($\text{Li}_{0.92}\text{FeF}_3$) rather than the intercalation of lithium, as lithium is a poor scatterer of X-rays. The proposal of an $R3c$ structure for $\text{Li}_{0.92}\text{FeF}_3$ is inspired by the fitting results of Fourier transforms of k^3 -weighted XAFS spectra (vide infra). During discharge from $x = 0.92$ to 2.78 Li, all Bragg peaks associated with the lithiated FeF_3 phase decreased in intensity; the new broadened peak at 44.7° with maximum intensity at $x = 2.78$ Li suggested the presence of the new phases LiF and Fe, which are the products of conversion reaction 3. However, the peaks of LiF are difficult to identify due to overlap with the (111) and (200) peaks of Al and the (110) peak of Fe. During the recharge to 4.5 V after first discharge, the (012), (113), and (116) peaks increase in intensity, and their positions revert to those of the initial FeF_3 , indicating that reactions 2 and 3 are reversible.

Figure 6 shows the Fourier transformed k^3 -weighted Fe K-edge XAFS spectra (the k -space XAFS spectra are shown in the Supporting Information) over the range of 3–13 \AA^{-1} . Spectra

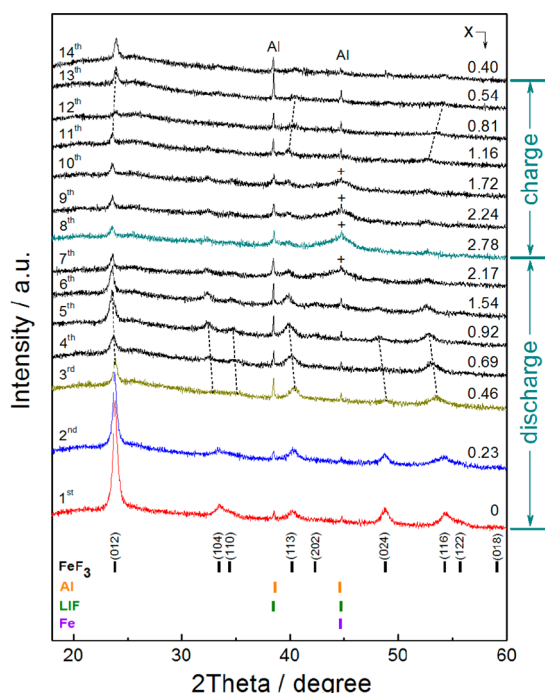


Figure 5. Ex situ XRD patterns of the FeF_3 cathode at specific states of discharge/charge. The bars on the bottom represent the positions of Bragg diffraction peaks corresponding to FeF_3 (PDF no. 00-033-0647), Al (PDF no. 00-001-1179), LiF (PDF no. 00-45-1460), and Fe (PDF no. 00-006-0696), respectively.

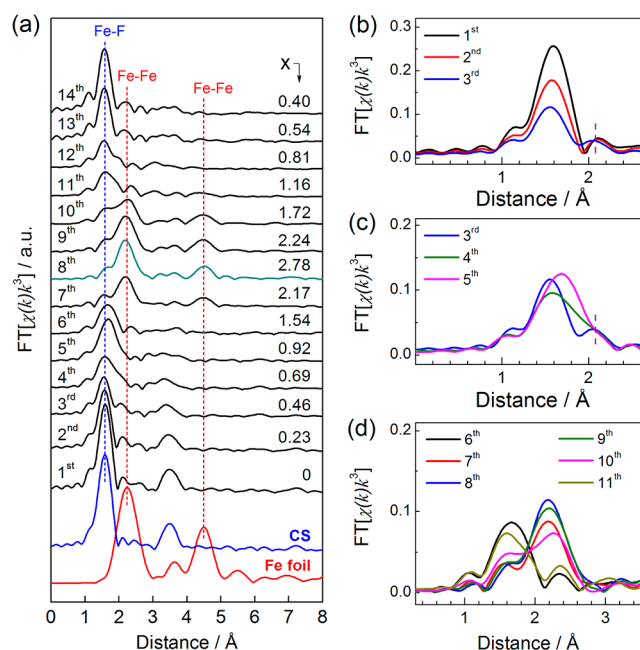


Figure 6. (a) Fourier transformed k^3 -weighted XAFS spectra of the FeF_3 cathode during first cycle and (b) overlay spectra 1st–3rd, (c) spectra 3rd–5th, and (d) spectra 6th–11th. The spectra of CS and Fe foil are also shown for comparison.

1st–3rd were very similar to each other, although their peak intensities were observed to decrease from one sample to the next. Spectra 4th–5th were clearly different from those which preceded them; the main peak at 1.93 \AA gradually broadened and shifted to a longer distance of $\sim 2.05 \text{ \AA}$. (See Figure 6b,c.) As for spectra 6th–8th, a new peak at 2.5 \AA (indexed to Fe–Fe,

see Figure 6a) appeared, indicating the formation of Fe metal, and increased in intensity to a maximum at $x = 2.78 \text{ Li}$. For spectra 9th–11th, the peak at 2.5 \AA decreased in intensity and disappeared at $x = 0.82 \text{ Li}$. An inverse relationship was observed between the intensities of the peaks at ca. 2.0 and 2.5 \AA for spectra 6th–11th (see Figure 6d), indicating conversion between different phases of the electrode material. As for spectra 12th–14th, the peak at 1.93 \AA again increased in intensity and reached a maximum at 4.5 V . The above observations are consistent with the phase changes suggested by ex situ XRD results (see Figure 5), and the reaction mechanism is described by reactions 2 and 3.

The coordination numbers (CN) and radial distances (R) of the Fe–F bond or Fe–Fe bond for lithiated FeF_3 were directly obtained by performing XAFS fitting using WinXAS software;³⁴ these parameters were instrumental in understanding the structural evolution of FeF_3 during cycling. XAFS spectra were fitted with one or more scattering paths, corresponding to Fe–F or Fe–Fe interactions, as required by the composition of the sample; these paths were generated using the ab initio program FEFF8³⁷ to compute scattering amplitude and phase-shift parameter values from the atomic coordinates of a model compound. To reduce the number of free-running parameters in the refinement to a reasonable level, it was necessary to make some assumptions about the samples. To this end, Debye–Waller factor (σ^2) values were correlated for spectra in which two distinct Fe–F environments were observed, and a single energy shift (ΔE_0) value was used for all paths in each spectrum. The correlation of σ^2 values for separate Fe–F paths is reasonable due to the fact that both exist in similar chemical environments and represent scattering from the same type of atom (i.e., fluorine). The assumption of a single ΔE_0 value for all paths is also valid, as it simply represents any experimental error in the assignment of E_0 during the preparation of the XAFS spectra for analysis.

The fitted Fourier transforms of k^3 -weighted XAFS spectra and the resulting parameter values are shown in the Supporting Information (see Figure S5 and Table S3); plots illustrating trends in these fitting parameters are shown in Figure 7. The reported uncertainties in fitting parameter values were computed from the corresponding off-diagonal elements of the correlation matrix. These values were weighted by the square root of the reduced χ^2 parameter of the fit to obtain the final values, taking into account the degree of shot noise in the Fourier transformed spectrum (sampled over the range 15 – 25 \AA , as recommended by Newville et al.³⁸).

According to the fitting results of XAFS spectra for Li_xFeF_3 ($x > 0.92 \text{ Li}$), the average Fe–Fe bond length of the formed Fe metal was $\sim 2.50 \text{ \AA}$, slightly longer than that of bulk Fe metal (2.482 \AA) (PDF no. 00-006-0696); the Fe–Fe CNs, however, were much lower than that of bulk Fe metal (the $\text{CN}_{\text{Fe–Fe}}$ of bulk Fe metal is 8). In fact, the large fraction of surface atoms in nanosized particles leads to a decrease in the average CN; in other words, the lower the CN, the smaller the particle size. The reduced CN values for these samples indicated that the formed Fe metal domains were nanosized, with the average size of these domains in $\text{Li}_{2.78}\text{FeF}_3$ being evaluated as $<1 \text{ nm}$ based on the work of Beale et al.³⁹ Because of the relatively large amount of non- Fe^0 material in the electrode at this point (e.g., the $\text{Li}_{2.78}\text{FeF}_3$ sample was composed of $\sim 24\%$ Fe, 73% LiF and 3% $\text{Li}_{0.92}\text{FeF}_3$, based on the amount of Li intercalation proceeding in reactions 2 and 3), the Fe^0 regions being formed could easily be separated from one another by a matrix of

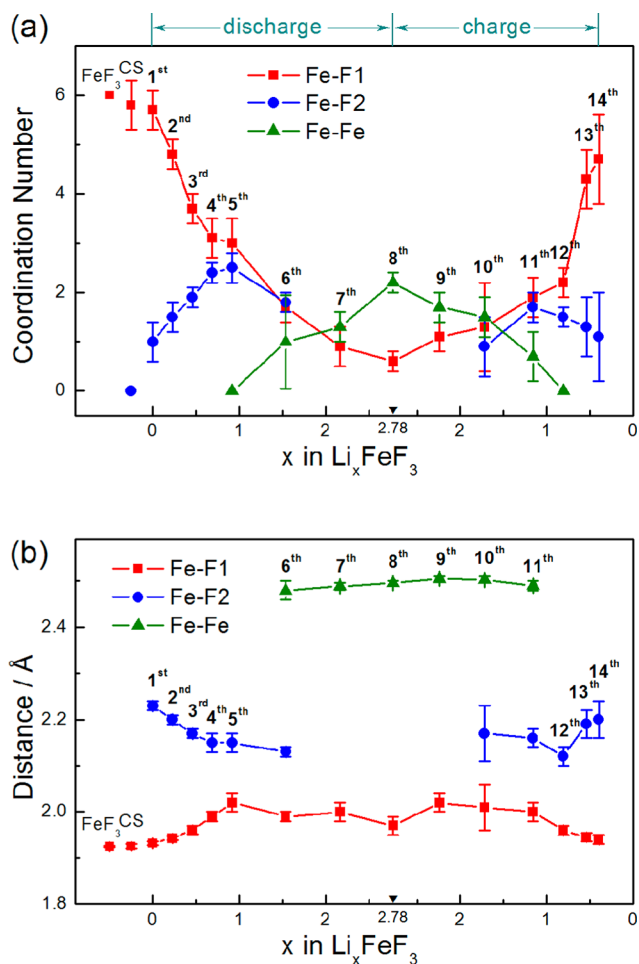


Figure 7. (a) CN and (b) R values obtained by XAFS fitting of the lithiated FeF_3 material.

$\text{Li}_{0.92}\text{FeF}_3$ and LiF . While shorter bond lengths are often observed in nanoparticles, this is due to bond contraction between atoms composing the surface and subsurface layers of the particle; as a result of the Fe^0 particles being formed while (presumably) surrounded by a matrix of $\text{Li}_{0.92}\text{FeF}_3$ and LiF , it is likely that the longer bond lengths observed are due to relatively strong interactions of the surface Fe^0 atoms with these surrounding matrix materials.

As shown in Figure 7, the Fe-F bond lengths for the lithiated FeF_3 diverged into two distinct groups upon discharging. These groups ($R_{\text{Fe-F1}}$ and $R_{\text{Fe-F2}}$) appeared to converge toward ca. 2.0 and 2.15 Å, respectively, when x reached 0.92 Li. While the Fe-F bond lengths varied with x in Li_xFeF_3 , the Fe-F CNs also varied. It is worthwhile to note that the total Fe-F CNs (i.e., the sums of $\text{CN}_{\text{Fe-F1}}$ and $\text{CN}_{\text{Fe-F2}}$) for all Li_xFeF_3 ($x = 0.23, 0.46, 0.69$, or 0.92) samples were nearly 6. By analyzing XRD patterns of Li_xFeF_3 ($x = 0$ to 1.0 Li) similar to those shown in Figure 5, Yamakawa et al.⁵ suggested that the similarity in peak positions for FeF_3 and Li_xFeF_3 may indicate that some structural motifs are common to the two phases. In other words, the structural evolution occurring in the range of $x = 0$ to 1.0 Li is moderate, and the Fe or F atoms may move very little within the lattice (consistent with the XAFS fitting results).

The total Fe-F CNs of the Li_xFeF_3 ($x = 1.54$ to 2.78 Li) samples decreased with the increase in x ; this is associated with the formation of Fe metal nanoparticles as the discharge nears completion. There should be little to no Fe-F bonding in the Fe metal phase, but because the total Fe-F CN is an average over all Fe atoms within the sample this contribution from the Li_xFeF_3 phase is still observed. For example, because the $\text{Li}_{1.54}\text{FeF}_3$ sample was composed of ca. 70% $\text{Li}_{0.92}\text{FeF}_3$ and ca. 30% Fe, the total Fe-F CN of $\text{Li}_{1.54}\text{FeF}_3$ is expected to be ca. 70% of that of $\text{Li}_{0.92}\text{FeF}_3$ (consistent with the fitting results shown in Table S2 in the Supporting Information). When the $\text{Li}_{0.92}\text{FeF}_3$ levels are low in the Li_xFeF_3 (e.g., $x = 2.17$ to 2.78), however, the CNs determined by fitting the Li_xFeF_3 data seem to deviate somewhat from the expected values; this may be the result of the fact that only a single Fe-F scattering path could be included in these fits due to the reduced intensity of the Fe-F peak. On charging to 4.5 V after the first discharge of the cell, the total Fe-F CNs reverted to nearly six, again indicating the reversibility of reactions 2 and 3.

According to Figure 7, upon discharging from $x = 0$ to 0.92 Li, the $\text{CN}_{\text{Fe-F1}}$ and $\text{CN}_{\text{Fe-F2}}$ values of the lithiated FeF_3 gradually converged toward a value of 3 as the sample composition approached $x = 0.92$ Li. It is the observation that $R_{\text{Fe-F1}} \neq R_{\text{Fe-F2}}$ and $\text{CN}_{\text{Fe-F1}} \approx \text{CN}_{\text{Fe-F2}}$ that inspires the proposition that the space group of $\text{Li}_{0.92}\text{FeF}_3$ is $R3c$, as seen in LiNbO_3 (PDF no. 00-020-0631). The structural evolution from $R-3c$ (FeF_3) to $R3c$ ($\text{Li}_{0.92}\text{FeF}_3$) is depicted in Figure 8 and is based on those parameters extracted from the corresponding

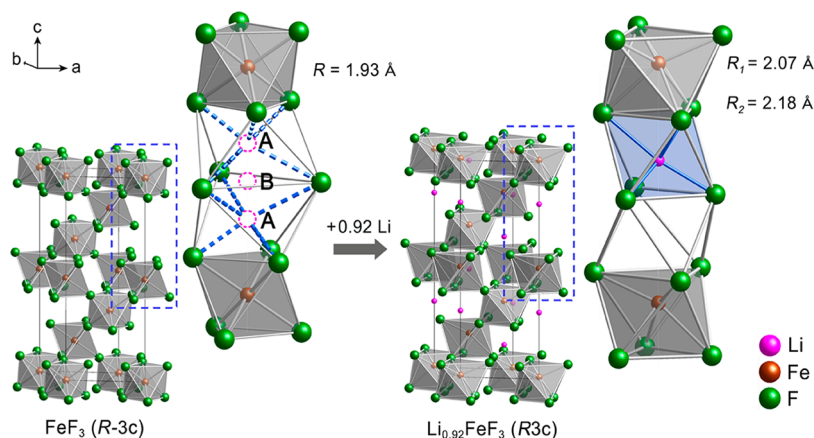


Figure 8. Structural schemes of FeF_3 ($R-3c$) and $\text{Li}_{0.92}\text{FeF}_3$ ($R3c$).

Table 1. Cell and Atomic Parameters of FeF₃ and Li_{0.92}FeF₃^a

chemical formula	space group	cell parameter			atomic parameter			
		a/Å	c/Å	V/Å ³	atom	site	occupancy	x, y, z
FeF ₃	R-3c	5.2239(6)	13.2854(12)	313.97(10)	Fe	6b	1.0	0.0000, 0.0000, 0.0000
					F	18e	1.0	0.0000, 0.4114(5), 0.7500
Li _{0.92} FeF ₃	R3c	5.1443(7)	14.0125(13)	321.15(10)	Fe	6a	1.0	0.0000, 0.0000, 0.0087(6)
					F	18b	1.0	0.0054(7), 0.3706(12), 0.0697(4)
					Li	6a	0.92	0.0000, 0.0000, 0.3062(5)

^a*wRp*, *Rp*, and χ^2 for the refinement of Li_{0.92}FeF₃ were 1.83%, 1.52%, and 1.003, respectively.

XRD patterns (see Table 1) by Rietveld refinement with model structures of *R-3c* and *R3c* for FeF₃ and Li_{0.92}FeF₃, respectively.

In the crystal structure of FeF₃ with the space group *R-3c*, each iron atom is coordinated to six fluorine atoms forming a FeF₆ octahedron, which connects in turn with neighboring octahedra via corner-sharing of fluorine atoms to form a 3D framework. (See Figure 8.) Between two FeF₆ octahedra along the *c* axis there is an elliptic-like space that has two possible vacancy sites for the intercalation of lithium ions during discharge (designated herein as 'A' and 'B', see Figure 8). XRD Rietveld refinement revealed that lithium ions preferentially occupied 'A' sites rather than 'B' sites in the electrode material; this ordered distribution of lithium ions in site 'A' leads to the breaking of centric symmetry in the *R-3c* structure and in turn results in the formation of the acentric *R3c* space group for Li_{0.92}FeF₃. The crystal structure of Li_{0.92}FeF₃ can thus be envisaged as a 3D framework built by two distinct sets of FeF₆ octahedra and LiF₆ octahedra. The two sets of octahedra interconnect via sharing corners, edges, and faces, generating a complex 3D framework. It should be noted that the arrangement of alternating face-sharing octahedral FeLiF₉ dimers and vacancy octahedra along the *c* axis is quite common, as observed in corundum Al₂O₃ (PDF no. 00-001-1296). It is also important to note that the Li atom is not exactly in the middle of two FeF₆ octahedra but biases toward one of the two, resulting in a reduction of lattice symmetry (from *R-3c* to *R3c*) and the splitting of Fe–F bond lengths. (The values of *R*₁ = 2.07 Å and *R*₂ = 2.18 Å shown in Figure 8 are consistent with those obtained from the XAFS fittings shown in Table S2 in the Supporting Information.) By comparison with the lattice constant of FeF₃, Li_{0.92}FeF₃ has a smaller *a* (or *b*) parameter and a larger *c* parameter. Upon discharging from *x* = 0 to 0.92 Li, the Fe³⁺ ions are reduced to Fe²⁺ and the attractive force between Fe and F is weakened, resulting in the increase in the Fe–F bond lengths. Meanwhile, the repulsive force between Fe and Fe is also weakened, resulting in a shrinking of the unit cell along the *a* axis (or *b* axis), whereas the increase in *c* is mainly derived from the preferred intercalation of Li in layers perpendicular to the *c* axis.

The structure of Li_{0.46}FeF₃ differs from that reported for Li_{0.5}FeF₃ with a *P4₂/mmn* (PDF no. 00-027-1246) or *P4₂nm* (PDF no. 01-084-1696) space group. The similarity of the XRD patterns for Li_{0.46}FeF₃ and Li_{0.92}FeF₃ (see Figure 5) suggests that they may have similar structures. However, Li_{0.46}FeF₃ must not be completely of the *R3c* space group because its CN_{Fe–F1} is not close to CN_{Fe–F2}. The structure of Li_{0.46}FeF₃ might thus be a transition structure between *R-3c* and *R3c*, such as *R3*. (See the Supporting Information for additional details.)

4. CONCLUSIONS

In situ XAFS techniques were used to analyze an FeF₃ electrode material sample at a series of potentials and proved to be a powerful tool in investigating the structural evolution of FeF₃ during the electrochemical cycling process. The XANES spectra provided abundant information regarding the reactions that occurred during the discharge/charge of FeF₃ cathode. The presence of two distinctive sets of isosbestic points, combined with the ex situ XRD analysis, revealed that the reaction of FeF₃ with Li proceeded in two steps: an intercalation reaction in the range of *x* = 0 to 0.92 Li and a conversion reaction in the range of *x* = 0.92 to 2.78 Li. Close inspection of the isosbestic points further revealed that the intercalation reaction actually comprises two stages: a two-phase intercalation reaction in the range of *x* = 0 to 0.46 Li, followed by a single-phase intercalation reaction in the range of *x* = 0.46 to 0.92 Li. On the basis of the fitting result of the Fourier-transformed XAFS spectra, the trends in Fe–F bond lengths and CN values were obtained. It was found that Fe–F bond lengths diverged basically into two groups, and that the total CN varied little in the range of *x* = 0 to 0.92 Li. Combined with the observation that *R*_{Fe–F1} ≠ *R*_{Fe–F2} and CN_{Fe–F1} ≈ CN_{Fe–F2} ≈ 3 for Li_{0.92}FeF₃, this supported the proposition that structural evolution of the electrode occurs from *R-3c* (FeF₃) to *R3c* (Li_{0.92}FeF₃) during discharge. The data also suggest that this process is reversible and may indicate the presence of an *R3* intermediate (i.e., Li_{0.46}FeF₃) as a transition structure between the *R-3c* and *R3c* phases. Finally, the average Fe–Fe CN of Li_{2.78}FeF₃ (ca. 2.2) was much lower than that of bulk Fe, indicating that the average diameter of the Fe domains formed during discharge were <1 nm.

■ ASSOCIATED CONTENT

Supporting Information

Synthesis of anhydrous FeF₃; physical characterization using XRD and SEM; preparation of the electrode; in situ cell for XAFS measurements; linear combination fittings (LCFs) of in situ XANES spectra; *k*-space XAFS spectra; fitted Fourier transforms of *k*³-weighted XAFS spectra; and discussion of the structure of Li_{0.46}FeF₃. This material is available free of charge via the Internet at <http://pubs.acs.org>.

■ AUTHOR INFORMATION

Corresponding Author

*E-mail: yyang@xmu.edu.cn; Tel/Fax: +86-592-218 5753 (Y.Y.). E-mail: peng.zhang@dal.ca; Tel.: +1-902-494 3323; Fax: +1-902-494 1310 (P.Z.).

Notes

The authors declare no competing financial interest.

■ ACKNOWLEDGMENTS

Financial support from the National Basic Research Program of China (973 program, grant no. 2011CB935903) and the National Natural Science Foundation of China (grant nos. 21233004, 21021002, and 20873115) is gratefully acknowledged. P.Z. thanks NSERC Canada for the XAFS analysis and simulation programs. In situ electrochemical XAFS were performed at beamline BL14W1 at the Shanghai Synchrotron Radiation Facility (SSRF), China.

■ REFERENCES

- (1) Armand, M.; Tarascon, J. M. Building Better Batteries. *Nature* **2008**, *451*, 652–657.
- (2) Bervas, M.; et al. Bismuth Fluoride Nanocomposite as a Positive Electrode Material for Rechargeable Lithium Batteries. *Electrochem. Solid-State Lett.* **2005**, *8*, A179–A183.
- (3) Badway, F.; et al. Carbon-Metal Fluoride Nanocomposites: Structure and Electrochemistry of $\text{FeF}_3\cdot\text{C}$. *J. Electrochem. Soc.* **2003**, *150*, A1209–A1218.
- (4) Amatucci, G. G.; Pereira, N. Fluoride Based Electrode Materials for Advanced Energy Storage Devices. *J. Fluorine Chem.* **2007**, *128*, 243–262.
- (5) Yamakawa, N.; et al. Identifying the Local Structures Formed during Lithiation of the Conversion Material, Iron Fluoride, in a Li Ion Battery: A Solid-State NMR, X-ray Diffraction, and Pair Distribution Function Analysis Study. *J. Am. Chem. Soc.* **2009**, *131*, 10525–10536.
- (6) Arai, H.; et al. Cathode Performance and Voltage Estimation of Metal Trihalides. *J. Power Sources* **1997**, *68*, 716–719.
- (7) Lachter, A.; Salardenne, J.; Barrière, A. S. Optical Absorption Study of Iron Trifluoride Thin Films. *Phys. Status Solidi B* **1978**, *90*, 147–150.
- (8) Pereira, N.; et al. Iron Oxyfluorides as High Capacity Cathode Materials for Lithium Batteries. *J. Electrochem. Soc.* **2009**, *156*, A407–A416.
- (9) Badway, F.; et al. Carbon Metal Fluoride Nanocomposites: High-Capacity Reversible Metal Fluoride Conversion Materials as Rechargeable Positive Electrodes for Li Batteries. *J. Electrochem. Soc.* **2003**, *150*, A1318–A1327.
- (10) Badway, F.; et al. Structure and Electrochemistry of Copper Fluoride Nanocomposites Utilizing Mixed Conducting Matrices. *Chem. Mater.* **2007**, *19*, 4129–4141.
- (11) Liu, L.; et al. Synthesis and Electrochemical Performance of Spherical FeF_3/ACMB composite as cathode material for lithium-ion Batteries. *J. Mater. Sci.* **2012**, *47*, 1819–1824.
- (12) Li, C.; et al. Low-Temperature Ionic-Liquid-Based Synthesis of Nanostructured Iron-Based Fluoride Cathodes for Lithium Batteries. *Adv. Mater.* **2010**, *22*, 3650–3654.
- (13) Li, C.; et al. A Mesoporous Iron-Based Fluoride Cathode of Tunnel Structure for Rechargeable Lithium Batteries. *Adv. Funct. Mater.* **2011**, *21*, 1391–1397.
- (14) Zhang, W.; et al. Synthesis and Characterization of in Situ Fe_2O_3 -Coated FeF_3 Cathode Materials for Rechargeable Lithium Batteries. *J. Mater. Chem.* **2012**, *22*, 24769–24775.
- (15) Poizot, P.; et al. Nano-Sized Transition-Metal Oxides As Negative-Electrode Materials for Lithium-Ion Batteries. *Nature* **2000**, *407*, 496–499.
- (16) Li, H.; Balaya, P.; Maier, J. Li-Storage via Heterogeneous Reaction in Selected Binary Metal Fluorides and Oxides. *J. Electrochem. Soc.* **2004**, *151*, A1878–A1885.
- (17) Teo, B. K. *EXAFS: Basic Principles and Data Analysis*; Berlin: Springer-Verlag, 1986.
- (18) Koeningsberger, D. C.; Prins, R. *X-ray Absorption: Principles, Applications and Techniques of EXAFS, SEXAFS, and XANES*; John Wiley & Sons: New York, 1988.
- (19) Rehr, J. J.; Albers, R. C. Theoretical Approaches to X-ray Absorption Fine Structure. *Rev. Mod. Phys.* **2000**, *72*, 621–654.
- (20) Song, M.-K.; et al. Nanostructured Electrodes for Lithium-Ion and Lithium-Air Batteries: The Latest Developments, Challenges, And Perspectives. *Mater. Sci. Eng., R* **2011**, *72*, 203–252.
- (21) Rougier, A.; Delmas, C.; Chadwick, A. V. Non-Cooperative Jahn-Teller Effect in LiNiO_2 : An EXAFS Study. *Solid State Commun.* **1995**, *94*, 123–127.
- (22) Nakai, I.; et al. X-ray Absorption Fine Structure and Neutron Diffraction Analyses of de-Intercalation Behavior in the LiCoO_2 and LiNiO_2 Systems. *J. Power Sources* **1997**, *68*, 536–539.
- (23) Shiraishi, Y.; et al. In situ Transmission X-Ray Absorption Fine Structure Analysis of the Charge-Discharge Process in LiMn_2O_4 , a Rechargeable Lithium Battery Material. *J. Solid State Chem.* **1997**, *133*, 587–590.
- (24) Giorgetti, M.; et al. Characterization of Sol-Gel-Synthesized LiFePO_4 by Multiple Scattering XAFS. *Inorg. Chem.* **2006**, *45*, 2750–2757.
- (25) Yoon, W.-S.; et al. Investigation of the Charge Compensation Mechanism on the Electrochemically Li-Ion Deintercalated $\text{Li}_{1-x}\text{Co}_{1/3}\text{Ni}_{1/3}\text{Mn}_{1/3}\text{O}_2$ Electrode System by Combination of Soft and Hard X-ray Absorption Spectroscopy. *J. Am. Chem. Soc.* **2005**, *127*, 17479–17487.
- (26) Arachi, Y.; et al. Structural Change of $\text{Li}_{1-x}\text{Ni}_{0.5}\text{Mn}_{0.5}\text{O}_2$ Cathode Materials for Lithium-ion Batteries by Synchrotron Radiation. *Chem. Lett.* **2003**, *32*, 60–61.
- (27) Nonaka, T.; et al. In situ XAFS and micro-XAFS Studies on $\text{LiNi}_{0.8}\text{Co}_{0.15}\text{Al}_{0.05}\text{O}_2$ Cathode Material for Lithium-Ion Batteries. *J. Power Sources* **2006**, *162*, 1329–1335.
- (28) Bervas, M.; et al. Investigation of the Lithiation and Delithiation Conversion Mechanisms of Bismuth Fluoride Nanocomposites. *J. Electrochem. Soc.* **2006**, *153*, A799–A808.
- (29) Mansour, A. N.; et al. In Situ X-ray Absorption Spectroscopic Investigation of the Electrochemical Conversion Reactions of $\text{CuF}_2\cdot\text{MoO}_3$ Nanocomposite. *J. Solid State Chem.* **2010**, *183*, 3029–3038.
- (30) Larson, A. C.; Dreele, R. B. V. *General Structure Analysis System (GSAS)*, Los Alamos National Laboratory Report LAUR 86-748, 2004.
- (31) Rosciano, F.; et al. A Multi-Sample Automatic System for in Situ Electrochemical X-ray Diffraction Synchrotron Measurements. *J. Synchrotron Radiat.* **2007**, *14*, 487–491.
- (32) *Introduction of BL14W1*. <http://ssrf.sinap.ac.cn/english/3/BL14W1.htm>.
- (33) Bearden, J. A. X-Ray Wavelengths. *Rev. Mod. Phys.* **1967**, *39*, 78–124.
- (34) Ressler, T. WinXAS: a Program for X-ray Absorption Spectroscopy Data Analysis under MS-Windows. *J. Synchrotron Radiat.* **1998**, *5*, 118–122.
- (35) Westre, T. E.; et al. A Multiplet Analysis of Fe K-Edge 1s \rightarrow 3d Pre-Edge Features of Iron Complexes. *J. Am. Chem. Soc.* **1997**, *119*, 6297–6314.
- (36) Jain, G.; Balasubramanian, M.; Xu, J. J. Structural Studies of Lithium Intercalation in a Nanocrystalline $\alpha\text{-Fe}_2\text{O}_3$ Compound. *Chem. Mater.* **2006**, *18*, 423–434.
- (37) Ankudinov, A. L.; et al. Real-Space Multiple-Scattering Calculation and Interpretation of X-ray-Absorption near-Edge Structure. *Phys. Rev. B* **1998**, *58*, 7565–7576.
- (38) Newville, M.; Boyanov, B. I.; Sayers, D. E. Estimation of Measurement Uncertainties in XAFS Data. *J. Synchrotron Radiat.* **1999**, *6*, 264–265.
- (39) Beale, A. M.; Weckhuysen, B. M. EXAFS As a Tool to Interrogate the Size and Shape of Mono and Bimetallic Catalytic Nanoparticles. *Phys. Chem. Chem. Phys.* **2010**, *12*, 5562–5574.